Interstitial defects in diamond: A quantum mechanical simulation of their EPR constants and vibrational spectra

Fabio Colasuonno, Francesco Silvio Gentile, William Mackrodt, et al.

View Online   Export Citation   CrossMark

Interstitial defects in diamond: A quantum mechanical simulation of their EPR constants and vibrational spectra

View Online   Export Citation   CrossMark

Fabio Colasuonno,[1] [ID] Francesco Silvio Gentile,[1,a)] [ID] William Mackrodt,[1] [ID] Anna Maria Ferrari,[1] [ID] Alexander Platonenko,[2] [ID] and Roberto Dovesi[1] [ID]

AFFILIATIONS

[1] Dipartimento di Chimica, Università di Torino and NIS (Nanostructured Interfaces and Surfaces) Centre,
Via P. Giuria 5, 10125 Torino, Italy

[2] Institute of Solid State Physics, University of Latvia, 8 Kengaraga Street, LV1063 Riga, Latvia

[a)]Author to whom correspondence should be addressed: francesco.gentile@unina.it

ABSTRACT

The local geometry, electronic structure, and vibrational features of three vicinal double interstitial defects in diamond, I_CI_C, I_CI_N, and I_NI_N, are investigated and compared with those of three "simple" $\langle 100 \rangle$ interstitial defects, I_{CC}, I_{CN}, and I_{NN}, previously reported by Salustro *et al.* [Phys. Chem. Chem. Phys. **20**, 16615 (2018)], using a similar quantum mechanical approach based on the B3LYP functional constructed from Gaussian-type basis sets, within a supercell scheme, as implemented in the CRYSTAL code. For the first time, the Fermi contact term and hyperfine coupling tensor $\mathcal{B}$ of the four open shell structures, I_CI_C, I_CI_N, I_{CC}, and I_{CN}, are evaluated and compared with the available experimental EPR data. For the two double interstitial defects, the agreement with experiment is good, whereas that for the single interstitials is found to be very poor, for which a likely reason is the incorrect attribution of the EPR spectra to uncertain atomic details of the microstructure of the samples. The infrared spectra of the three double interstitial defects exhibit at least two peaks that can be used for their characterization.

Published under license by AIP Publishing. https://doi.org/10.1063/5.0014368

I. INTRODUCTION

Natural and synthetic diamonds have attracted significant interest for many possible applications, such as high temperature diodes, transistors, thermistors, detectors, and windows for plasma heating in nuclear fusion power plants,[2–4] in view of their high melting point, thermal conductivity, hardness, and wide bandgap. The presence of intrinsic and extrinsic point defects in the crystalline lattice can dramatically modify some of the above properties so that over the last few decades, the investigation of both native and induced defects in diamond has been of continuing interest both from experimental and computational perspectives.[5–12] More recently, point defects in diamond have come into even sharper focus with the emergence and development of quantum dot devices based on diamond.[13,14] Among the intrinsic defects, the vacancy V[15–18] and $\langle 100 \rangle$ self-interstitial (see Fig. 1, top left, for the latter)[8,19–21] are the most common, and their formation and

recombination mechanisms have been investigated.[22,23] Of the possible impurities, nitrogen is by far the most common, in both synthetic and natural diamonds, with concentrations of thousands of parts per million (ppm) not uncommon.[24] One of the reasons for this is that nitrogen can be hosted relatively easily in the diamond lattice as a result of its atomic radius, which is very close to that of carbon. However, despite this, substitutional nitrogen, N_s, can lead to the displacement of a C atom to form a $\langle 100 \rangle$ interstitial as a result of the difference in the electronic configurations of C and N, where N_s is one of the two three-coordinated atoms of the interstitial. Thus, in the presence of nitrogen, three kinds of $\langle 100 \rangle$ interstitial defect (indicated here as I_{xy}, where x and y are the two threefold coordinated atoms) can, in principle, be found, namely, I_{CC}, I_{CN}, and I_{NN}. Furthermore, two I_{xy} defects can interact to generate a more stable structure, in which two three-coordinated atoms and two four-coordinated atoms form approximately square, planar structures (see Fig. 2), referred to
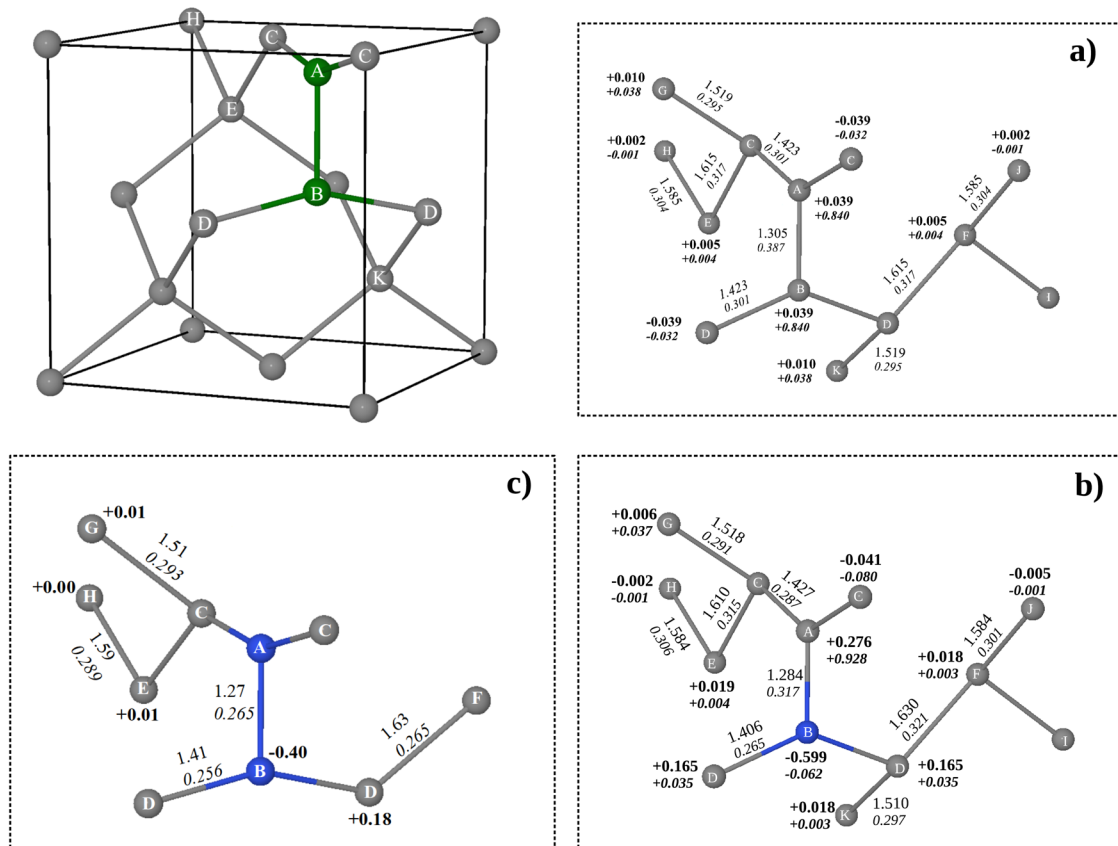
FIG. 1. Top left: The conventional diamond cell and interstitial I_{xy} defect (defect atoms in green). Panels (a), (b), and (c) refer to I_{CC}, I_{CN}, and I_{NN}, with nitrogen atoms in blue. Four numbers are shown in the schemes. Near the atoms, the atomic net charges q (top) and the magnetic moments μ (bottom) are shown. Along the bonds, the atom–atom distances R (top) and the bond populations b (bottom) are reported. Q and μ are in bold. b and R are in italic. q, μ, and b, as resulting from a Mulliken analysis, are given in $|e|$. R is in Å.

hereafter as I_xI_y. The two three-coordinated atoms are not first neighbors, as is the case for I_{xy}, which is probably the main reason for the higher stability of I_xI_y with respect to I_{xy}.

Relating experimental IR, Raman, or EPR spectra to a specific defect or a defect structure is fraught with difficulty and hence challenging, for it is essential to take into account the presence of other possible defects with potentially overlapping spectra. Computer simulations, on the other hand, are not subject to such difficulties, for the particular defect or defects in question are specified exactly *a priori*, in terms of their charge, spin, and multiplicity, if not the precise details of the defective lattice, so that there is always a 1:1 relationship between the defect and the computed spectra. Depending on the level of agreement with observation, these can then be used to validate, or otherwise, structures that have either been derived from or ascribed to the experimental spectra.

The purpose of the present paper, then, is twofold: the first is to report the predicted structures and EPR, IR, and Raman spectra of I_xI_y and I_{xy} defects obtained from quantum mechanical simulations and assess whether collectively or separately the spectra are sufficiently distinct for them to uniquely characterize the individual

defects; the second is to compare the computed and observed spectra, where available, and, in particular, the computed structures with those inferred from or ascribed to the spectra.

Only four of the six defects (I_CI_C, I_CI_N, I_{CC}, and I_{CN}), have neutral, open shell ground states and, hence, are EPR active. It is interesting to note, therefore, that four sets of EPR absorptions have been tentatively attributed to these defects, namely, I_CI_C(R1[25,26]), I_{CC}(R2[25]), I_CI_N(WAR10[27]), and I_{CN}(WAR9[27]).

All six compounds are IR and Raman active and could, therefore, in principle, be used to identify each of the defects.

In the present paper, all-electron quantum mechanical calculations based on the B3LYP functional utilizing Gaussian basis sets, and formulated within a supercell scheme,[28,29] have been used to study these six interstitial defects. This same approach has been used previously to investigate the structural and vibrational features of the three single interstitial defects, I_{xy}.[1,30] Here, we pay particular attention to the EPR spectra for I_CI_C, I_CI_N, I_{CC}, and I_{CN} and compare the computed data with experiment.

Recent applications to various defects (substitutional N, or N_s,[31] VN_2^-,[32] N_2^+[33]) have confirmed that the present approach is able
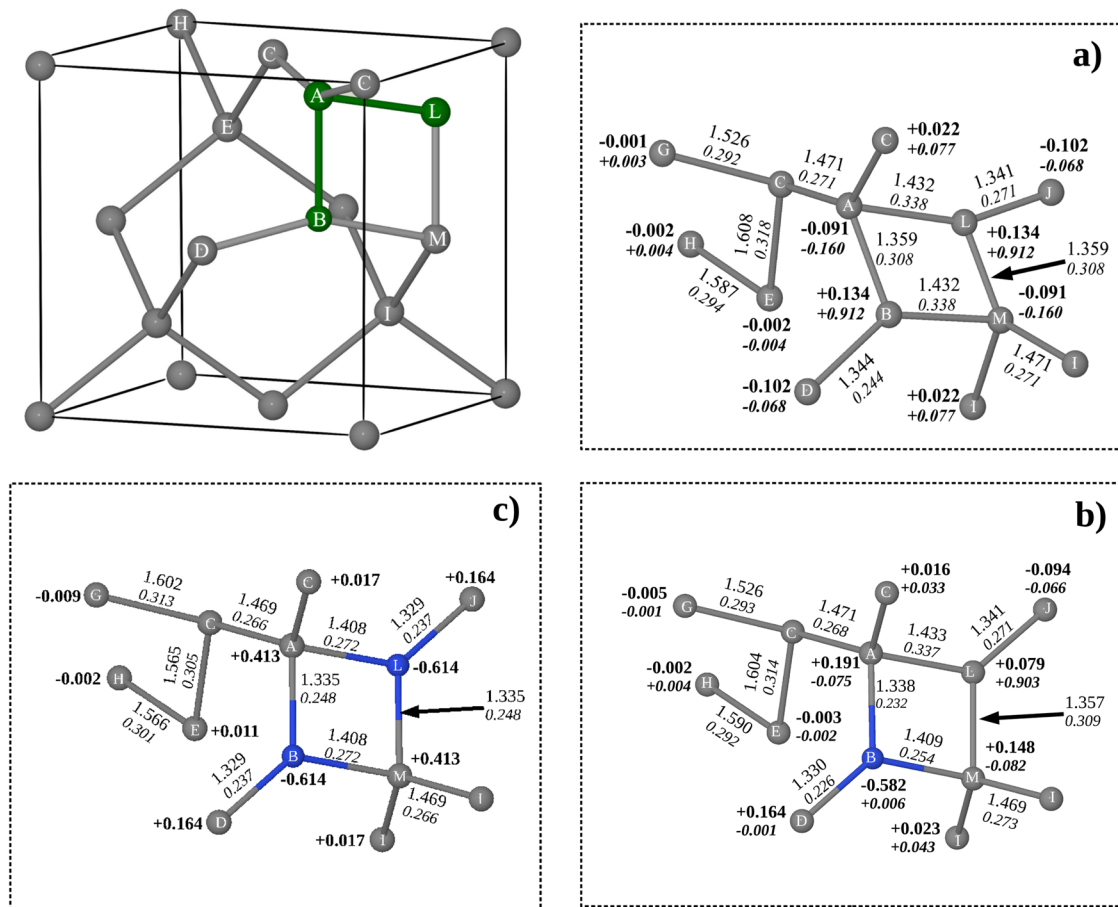
FIG. 2. Top left: The conventional diamond cell and interstitial $I_x I_y$ defect (defect atoms in green). Panels (a), (b), and (c) refer to $I_C I_C$, $I_C I_N$, and $I_N I_N$, respectively. Nitrogen atoms are in blue. Symbols and other information as in Fig. 1.

to provide an excellent agreement with the experimental EPR results, when the latter have been accurately determined.

This paper is structured as follows: Sec. II describes the computational methods used in this study. Section III contains the results and is organized in three parts. Subsection III A is devoted to the equilibrium geometries, charge and spin distributions, and band structures. Subsection III B reports the computed hyperfine coupling tensors and compares them with the available experimental data, while Subsection III C describes the vibrational features of these defects; finally, Sec. IV discusses the possible identification of the six I_{xy} and $I_x I_y$ defects through their EPR and/or IR spectra and draws some tentative conclusions.

II. COMPUTATIONAL METHODS

Calculations have been performed by using the B3LYP global hybrid functional[34,35] based on Pople's *all electron* 6-21G[36] basis sets of Gaussian-type functions, except for the exponents of the most diffuse sp shells of carbon and nitrogen, for which values of 0.23 bohr^{-2} and 0.30 bohr^{-2} have been adopted. However, a much

richer (and more expensive) basis set,[37] containing 6s shells, with 811 111 contractions of primitive functions, 2p shells, with 41 contractions, and 1d shell, with a total 17 atomic orbitals (AOs) per atom, has been adopted for the EPR calculations. This compares with the 9 AOs/atom of the smaller basis set. The enlarged set was originally derived from the standard 6-31G version, and although it was later extended, it is here referred to as 6-31G-J*. It was designed to better describe the core electrons, but the valence shells are also richer, with exponents of the most diffuse s and p functions of C and N set to 0.169 bohr^{-2} and 0.212 bohr^{-2}, respectively.[37]

This combination of the B3LYP functional and the 6-31G-J* basis set has been shown to provide accurate results for the EPR data of three defects in diamond, namely, N_s,[31] VN_2^- (the negatively charged form of VN_2, with two nitrogen atoms around a vacancy),[32] and N_2^+, the positively charged form of the so called A defect (two vicinal substitutional N atoms),[33] where in all three cases, the spin state is a doublet.

The Coulomb and exchange infinite lattice series are controlled by five parameters, T_i, which have been set to 8 (T_1–T_4) and 16 (T_5). The convergence threshold on the SCF energy was set to

10^{-8} hartree for structural optimizations and to 10^{-10} hartree for vibration frequency calculations.

A cubic supercell containing 216 (S_{216}) atoms has been considered.

The DFT exchange–correlation contribution and its gradient were evaluated by numerical integration over the unit cell volume. The generation of the integration grid points was based on an atomic partition method, originally developed by Becke[38] for molecules and further extended to periodic systems.[28,29] Within this scheme, the unit cell is partitioned into atomic volumes centered on the nuclei, where each point has an associated weight. The radial and angular points for the integration grid are generated using a Gauss–Legendre quadrature and Lebedev two-dimensional distribution, respectively. The choice of a suitable grid is crucial both for numerical accuracy and the optimization of computational resources. In this study, a pruned grid with 75 radial and 974 angular points has been used, whose accuracy can be measured by comparing the integrated charge density of $N_i = 1309.016$ for $I_{C}I_{N}$, with the total number of 1309 electrons in the unit cell. A Γ-point centered Pack–Monkhorst grid[39] for sampling reciprocal space has been used, consisting of $2 \times 2 \times 2 = 8$ (S_{216}) $\mathbf{k}$-points in the first Brillouin Zone. Harmonic phonon frequencies, ω_p, at the Γ point, the only point that contributes to the IR spectrum, were obtained from the diagonalization of the mass-weighted Hessian matrix of the second energy derivatives with respect to atomic displacements u,[40]

$$W^\Gamma_{ai,bj} = \frac{H^0_{ai,bj}}{\sqrt{M_a M_b}} \quad \text{with} \quad H^0_{ai,bj} = \left(\frac{\partial^2 E}{\partial u^0_{ai} \partial u^0_{bj}} \right), \quad (1)$$

where atoms a and b (with atomic masses M_a and M_b) in the reference cell, $\mathbf{0}$, are displaced along the ith and jth Cartesian directions, respectively. First-order derivatives were computed analytically, whereas second order derivatives were obtained numerically, using a two-point formula based on the difference between the gradient at the equilibrium position and that after a displacement of 0.003 bohr, along each Cartesian coordinate. It is important to note that as the optimization of the structure is a numerical process, the gradient at equilibrium is not exactly null but simply lower than the selected thresholds of the optimizer. Integrated intensities for IR absorption $\mathcal{I}_p$ are computed for each mode p using a computational scheme[41] based on the Berry phase,[42] wherein the derivatives of the dipole moment with respect to the Cartesian coordinates of the unit cell atoms are evaluated numerically in a similar way to that used for the numerical derivative of the energy gradient in obtaining the Hessian matrix. The IR spectrum is then computed from the Γ-point transverse-optic (TO) modes and the adoption of a pseudo-Voigt functional form consisting of Lorentzian curves with a full width at half maximum of 8 cm^{-1}.

The coupling between the unpaired electron spin ($\mathbf{S}$) and the system of the nuclear spins ($\mathbf{I}$) is described through the spin Hamiltonian

$$H = \sum_n \mathbf{S} \cdot \mathcal{A}^n \cdot \mathbf{I}^n, \quad (2)$$

where $\mathbf{I}^n$ and $\mathcal{A}^n$ refer to the nuclear spin and hyperfine coupling tensor related to the nth nucleus, at site $\mathbf{R}_n$, respectively. $\mathcal{A}^n$ can be written in the form

$$\mathcal{A}^n = A^n_{iso} \cdot I + \mathcal{B}^n, \quad (3)$$

where I is a 3×3 identity matrix, or

$$A^n_{ij} = A^n_{iso} \delta_{ij} + B^n_{ij}, \quad (4)$$

where A^n_{iso} is the isotropic contribution to $\mathcal{A}^n$, often referred to as the *Fermi contact term*, and $\mathcal{B}^n$ is the anisotropic dipole–dipole interaction of the electron and nuclear spins. The Fermi contact term for n unpaired electrons of total spin S_z,

$$A^n_{iso} = g_e \mu_e g_n \mu_N \frac{4\pi}{3 S_z} |\psi(\mathbf{R}_n)|^2 \quad (5)$$

relates to the direct interaction of nuclear and electron spins and is only non-zero for states with finite electron spin density, $|\psi(\mathbf{R}_n)|^2$, at nuclear sites $\mathbf{R}_n$, namely, those with unpaired electrons in s-subshells with S the spin state of the system. g_e, μ_e, g_n, and μ_N are the free-electron g-factor, Bohr magneton, gyromagnetic ratio of $\mathbf{I}^n$, and nuclear magneton, respectively. The elements of the traceless tensor $\mathcal{B}^n$ at nucleus $\mathbf{R}_n$ are defined by

$$B^n_{ij} = g_e \mu_e g_n \mu_N \frac{1}{2 S_z} \int d\mathbf{r}_n |\psi(\mathbf{r}_n)|^2 \left(\frac{3\mathbf{r}_{ni}\mathbf{r}_{nj} - |\mathbf{r}_n|^2 \delta_{ij}}{|\mathbf{r}_n|^5} \right), \quad (6)$$

where $\mathbf{r}_n$ is the distance to $\mathbf{R}_n$. $\mathcal{B}^n$ is usually written in terms of its three (principal axes) eigenvalues, B^n_1, B^n_2, and B^n_3, and is a measure of the unpaired electron populations of valence p and d orbitals centered on the magnetic nucleus and of all orbitals centered on neighboring atoms. Clearly, $A^n_{iso} = (A^n_1 + A^n_2 + A^n_3)/3$ since $\mathcal{B}^n$ is traceless, and, for a nuclear site with axial symmetry, we have $A^n_{iso} = (A^n_\parallel + 2A^n_\perp)/3$ and $B^n_\parallel + 2B^n_\perp = 0$.

When the local point symmetry of an atom is sufficiently low, the $\mathcal{B}^n$ tensor is not diagonal. Diagonalization, then, generates the eigenvalues, referred to above, and the eigenvectors that define the orientation of the $\mathcal{B}^n$ principal axes with respect to the Cartesian frame. This relative orientation is usually expressed in terms of the angles θ and φ formed by the largest $\mathbf{B}$ eigenvector and the $\langle 100 \rangle$ and $\langle 001 \rangle$ crystallographic directions, respectively.

An important point to note, especially with regard to electronic structure calculations, is that A^n_{iso} and B^n_{ij} impose different requirements on the wavefunction, for whereas A^n_{iso} is determined by the electron density at the nuclear positions, as indicated in Eq. (5), B^n_{ij} samples the long-range properties of the wavefunction as a result of the r^{-3} scaling in the integrand in Eq. (6). It is essential, therefore, for basis sets to be sufficiently flexible so that these differing dependencies can be satisfied.

III. RESULTS

A. Geometry, charge distribution, formation energy, and band structure

The electronic, structural, and vibrational properties of I_{xy} defects have been investigated previously[1,30] using the same basis set, DFT functional, computational conditions, and computer code (CRYSTAL). Here, we summarize the main results of this study, both for the purposes of comparison with the present results and to extend the analysis to the EPR constants, which were not investigated therein.

In the case of the single (split $\langle 001 \rangle$) interstitial defects, the two *interstitial atoms* are three-coordinated[43] so that in the case of I_{NN}, the ground state is a closed shell, with a covalent bond between the two N atoms at an internuclear distance of 1.27 Å and a Mulliken bond population of +0.265 $|e|$. The net charge on N is −0.40 $|e|$, which is nearly exactly compensated by charges of +0.18 × 2 $|e|$ at atoms D and C (see Fig. 1). The lone pairs of the two nitrogen atoms point in an orthogonal direction to the ACC and BDD planes, respectively.

In I_{CN}, the defective carbon atom contains an unpaired electron, with a calculated magnetic moment, μ, of +0.928 $|e|$, so that the ground state is a doublet ($S_z = 1/2$) and hence EPR active. The N–C distance is 1.28 Å, leading to a strong covalent bond (bond population +0.317 $|e|$) and net charges of +0.276 $|e|$ and −0.599 $|e|$ on C and N, respectively, while the charge on atom D, which is first neighbor to N, is +0.17 $|e|$. Overall, the perturbation of the charge distribution, from that in pristine diamond, is found to be very local.[30]

In terms of spin pairing alone, the unpaired electrons on the two defect carbon atoms in I_{CC} might seem suitable for bond formation. However, as shown in Fig. 1, the ACC and BDD planes, which contain the two unpaired electrons, are orthogonal so that covalent coupling cannot occur. Despite the short internuclear separation of 1.30 Å, the interaction between the two unpaired electrons is very weak, giving rise to a singlet state, which is more stable than the triplet by only 0.027 eV (313 K). The magnetic moments of the two spin states, μ, are identical (0.840 $|e|$) and the bond population, +0.387 $|e|$, indicates a strong covalent bond. The net charge q on the two three-coordinated carbon atoms is +0.039 $|e|$.

The large difference in polarity of the CN and CC bonds has important consequences for the intensity of the active IR modes, as shown below.

The top left panel of Fig. 2 shows the conventional diamond lattice containing the double interstitial defect. The four atoms involved in the defect are indicated as A, B, L, and M: A and M are in all cases carbon atoms and are fourfold coordinated; B and L are threefold coordinated and can be both N ($I_N I_N$), both C ($I_C I_C$), or one C and one N ($I_C I_N$). N atoms are shown in blue. It is likely that two of the defects, $I_C I_N$ and $I_C I_C$, were detected by Felton *et al.*,[27] Twitchen *et al.*,[26] and Hunt *et al.*,[25] where they were named WAR10 and R1, respectively. In the case of $I_N I_N$, on the other hand, we were unable to find any experimental evidence for its existence.

The equilibrium geometry of the three defects is shown in panels (a), (b), and (c) of Fig. 2.

As in the case of the *single* interstitial, when the two *defect* atoms, B and L, are nitrogen, the ground state is a closed shell; when one atom is C and the other is N [atom L in panel (b) of Fig. 2], the ground state is a doublet, with a single unpaired electron (μ = +0.903 $|e|$); finally, when B and L are both carbon atoms, the two unpaired electrons can form a triplet ($S_z = 1$), which is shown in panel (a) of Fig. 2, or an *open shell* singlet ($S_z = 0$), where the former is found to be the more stable by 0.034 eV. The open shell nature of the singlet is reflected in the magnetic moment, μ (+0.912 $|e|$), which is identical to that in the triplet state. The reason for the reversed order of stability of the singlet and triplet states in I_{CC} and $I_C I_C$ lies in the much shorter distance between the sites containing the unpaired electrons in I_{CC}, for at shorter distances, i.e., greater confinement, the singlet state is always favored over the triplet by virtue of the reduced Pauli repulsion between electrons of opposite spin.

Spin density maps in planes containing the interstitial atoms in $I_C I_N$ and $I_C I_C$ are shown in Fig. 4, in which the very strong spin localization at the three-coordinated carbon atom(s), the low spin density at N, and the spin polarization of the first neighbors of the defect atoms are clearly evident.

The formation energies, E_f^i, of the three double interstitial defects are reported in Table I. For future and cross comparison, we provide three definitions of E_f, identified by the superscript, *i*, although only the third one is briefly discussed here. A systematic discussion of the mechanism and energetic of the defect formation is beyond the scope of the present paper, mainly focused on the identification of the defects through the EPR signal.

E_f^1 and E_f^2 are defined through the following reaction:

$$\text{Diamond} + b \cdot \text{B} + l \cdot \text{L} \rightarrow \text{I}_B \text{I}_L.$$
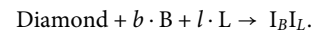
Atoms B and L can be both C or N with the restriction that $b + l = 2$. E_f^1 is calculated with reference to the isolated C and N atoms, with energies of −38.0559 E_h and −54.5228 E_h, respectively, while E_f^2 is calculated with respect to $1/2 N_2$ and the C atom in diamond, where the reference energies are −37.8106 E_h and −54.6563 E_h. E_f^3 is the formation energy of the double interstitial defects, which is computed as $E_f^3 = E(I_x I_y) − E(I_{xy}^1) − E(I_{xy}^2)$, where I_{xy}^1 and I_{xy}^2 are defined in columns 5 and 6 of the table. The energies of the single interstitial defects are −8257.7081 E_h, −8274.3809 E_h, and −8252.9898 E_h for I_{CC}, I_{CN}, and I_{NN}, respectively. In every case, the I_x–I_y defects are more stable than the two constituent defects, I_{xy}, by about 6 eV. This is supported by the experimental observation that to obtain double interstitial defects, it is sufficient to reach high concentrations of single interstitial defects in the host lattice. This is not surprising since combining two defects, each with two threefold coordinated atoms, results in a single defect with only two three-coordinated atoms.

The band structures of the three I_x–I_y defects are collected in Fig. 3, where the continuous black and dotted red lines indicate α and β bands, respectively, and the horizontal blue line represents the Fermi level (E_F). For the closed-shell system, $I_N I_N$, the α and β bands coincide. We note that the gap of perfect diamond, derived from the present functional and basis set, is 5.73 eV, which compares favourably with the experimental value of 5.80 eV.[44] In all three panels, energy differences refer to the Γ point, while the vertical excitations from the highest occupied defect levels to the lower edge of the conduction band (CBLE) are indicated by orange arrows. In the case of the $I_N I_N$ (right panel of Fig. 3), the energies of the two lone

TABLE I. Formation energies (in eV) of the I_x–I_y defects, computed with reference to the isolated atoms (E_f^1), to the N_2 molecule and diamond (E_f^2), or to the combination of two interstitial defects I_{xy}^1 and I_{xy}^2 (E_f^3). The total energy of the corresponding pristine diamond supercell is −8220.078 66 E_h (−37.8106 E_h per carbon atom). The total energy, in E_h, of the defective S_{216} supercell is also reported.

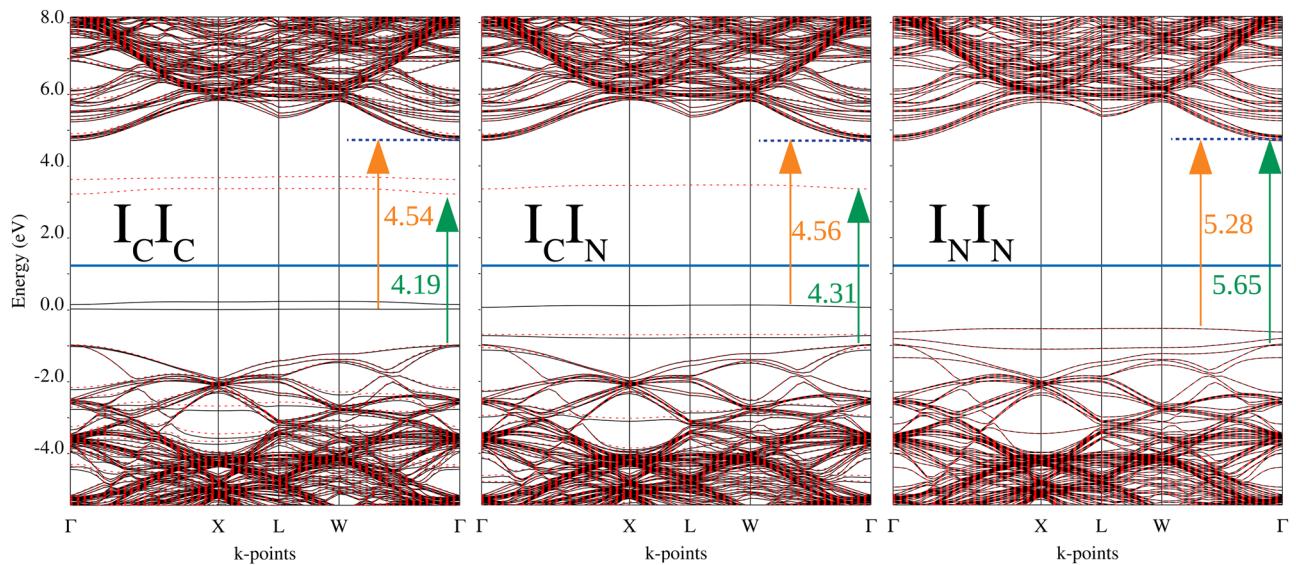| Defect	Total energy	E_f^1	E_f^2	I_{xy}^1	I_{xy}^2	E_f^3
$I_C I_C$	−8295.552 20	17.37	4.02	I_{CC}	I_{CC}	−5.84
$I_C I_N$	−8312.232 66	15.19	5.03	I_{CC}	I_{CN}	−6.04
$I_N I_N$	−8328.913 16	13.01	6.05	I_{CN}	I_{CN}	−6.26

FIG. 3. Band structures of I_CI_C (left), I_CI_N (central), and I_NI_N (right). The blue line represents the Fermi energy level. Continuous and dashed lines indicate α and β bands, respectively. Vertical arrows indicate the energy difference between the top of the valence band and the lowest unoccupied defect level (green) and between the lowest occupied defect level and the bottom of the conduction band (orange), both at the Γ point.

pairs of the nitrogen atoms are seen to be marginally above the top of the valence band (TVB) of the perfect system (0.34 eV and 0.15 eV) and the corresponding antibonding states, at the CBLE, leading to a vertical energy difference of 5.25 eV. The energy difference between the top of the valence band (TVB) and the lowest unoccupied state is shown in green, where the value, 5.65 eV, is 0.08 eV smaller than the gap in pristine diamond. This lowering is due to the presence of one of the antibonding states of the nitrogen lone pairs.

In I_CI_N (central panel), the doubly occupied lone pair band of N lies 0.27 eV above the TVB, while the (singly occupied) spin-band of the unpaired electron of the C atom is further 0.76 eV above at
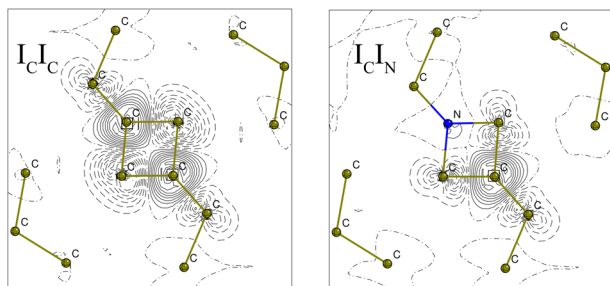

FIG. 4. Spin density maps for I_CI_C and I_CI_N in the plane through the four defect atoms that are coplanar. The spin density is truncated at $\pm 0.1|e|/a_0^3$, and the isodensity lines differ by $0.001|e|/a_0^3$. The continuous and dashed lines indicate positive and negative spin density values, respectively, while the dotted-dashed line indicates for zero spin density. The alternation of positive and negative spin density should be noticed, which propagates also to the neighbors of the defect atoms.

1.03 eV. The empty spin-band of the unpaired electron is in the gap, 1.33 eV below the BCB, leading to an excitation energy of 4.56 eV for the unpaired electron and one of 4.31 eV for an excitation from the top of the valence band. The resulting local bandgap is 5.59 eV, a reduction of 0.14 eV from the host lattice. Finally, as shown in the left panel of Fig. 3, in I_CI_C, the two unpaired C electrons occupy nearly degenerate spin states, split by 0.20 eV, 1.00 eV above the TVB, with the corresponding empty levels (one α and one β), separated by 0.42 eV, ~1.11 eV below the conduction band. This leads to a local narrowing of the bandgap to 5.65 eV.

B. The hyperfine coupling tensor

Our calculated EPR results for the four interstitial defects are reported in Table II, together with the experimental data, which have been attributed specifically to each of the defects. The first point to note is that the Fermi contact term, A_{iso}, and the components of the B tensor for I_CI_C (R1) and I_{CC} (R2) are much larger than those for the two other interstitials by up to two orders of magnitude.

In the I_CI_C case (first line in Table II), the calculated values of A_{iso}, B1, B2, and B3 are all close to the experimental values collected by Hunt et al.,[25] with a difference of 12% between the calculated (+49 MHz) and experimental (+43 MHz) values of the contact term and differences of 3.5%, 0.8%, and 0.8% for the three principal components of B, where the largest of these is +74 MHz from the experiment compared with the simulated value of +76 MHz. There is also very good agreement for the angles, θ and φ (see Sec. II for definitions). It is worth noting that for this defect, there are no uncertainties as to the identity of the local structures responsible for the EPR measurements.

For the ⟨100⟩ I_{CC} defect, the reported experimental data are very similar to those for I_CI_C, namely, +78 MHz, −39 MHz, and

TABLE II. Experimental and calculated isotropic and anisotropic components of the hyperfine coupling tensor. Expt. name indicates the name attributed by the experimental group to the defect. θ and φ are the angles between the principal axis of the B tensor and the $\langle 100 \rangle$ and $\langle 001 \rangle$ crystallographic directions. The results are for a S_{216} supercell.

Atom	A_{iso}	B_1	B_2	B_3	θ	φ	Expt. name	References
^{13}C in $I_C I_C$	49.0	73.9	37.0	37.0	90	315	R1	25 and 26
	+43.41	+76.47	−37.29	−39.18	90.00	314.67		This work
^{13}C in I_{CC}	+44	+78	−39	−39	ND	ND	R2	25
	+25.38	+76.34	−38.66	−37.68	90.00	90.00		This work
^{15}N in $I_C I_N$	0.00	−1.01	+1.00	0.00	134.82	45.00	WAR10	27
	−2.55	−1.40	+0.87	+0.53	134.80	45.00		This work
^{15}N in I_{CN}	+8.10	−0.25	+0.20	+0.07	90.00	45.00	WAR9	27
	+14.30	+1.77	−1.74	−0.034	89.98	45.00		This work

−39 MHz compared with +74 MHz, −37 MHz, and −37 MHz, respectively, for the B tensor and 44 MHz as opposed to 49 MHz for A_{iso}. There appears to be no reports for the angles, θ and φ, for I_{CC}. Now, the computed values of the I_{CC} B tensor are very close to those of $I_C I_C$, with the largest component of B, for example, 76 MHz in both cases. The calculated values of A_{iso}, on the other hand, are quite different, for the $I_C I_C$ value is +43 MHz and only +25 MHz in I_{CC}, which is a difference of 53%. There are two possible explanations for this apparent discrepancy. One is that the experimental data for the two defects are so close because they have been wrongly attributed and that, in fact, both sets of experiments refer to the same defect. The other is that the spectra of the two defects are indeed extremely similar and that the discrepancy between the experimental and simulated values of A_{iso}, +44 MHz and +25 MHz, respectively, is the result of inaccuracies in the calculations. We suggest that the first of these explanations is more likely for the following reasons:

- There is good agreement between the experimental and calculated values of A_{iso} for $I_C I_C$, which, from the point of view of the present computational techniques *per se*, is similar to, though not, of course, identical to I_{CC}, so that it is entirely reasonable to expect similar errors for the two defects.
- Hunt *et al.* have emphasized that *all the experimental values are approximate* because of the uncertainties in deconvoluting the various linewidths.[45] For these reasons, we posit that the experimental results attributed to I_{CC} are, in fact, for $I_C I_C$.

Turning now to the heteronuclear double interstitial, $I_C I_N$, evaluating the EPR constants is difficult on two counts. The first is that the natural abundance of ^{15}N is only 0.4%; the second is that the comparatively large distance between N and the C atom bearing the unpaired electron, 1.86 Å, leads to constants whose absolute magnitudes are very small. Thus, an experimental value of zero has been reported for A_{iso},[27] whereas the present calculations predict one of −2.5 MHz. It is worth noting, however, that the absolute difference between the simulated and experimental values is smaller than that for $I_C I_C$ (6 MHz). The components of the B tensor are, likewise, very

small, but here, the measured and calculated constants are of similar magnitude and sign, with values of −1.01 MHz and −1.40 MHz for B1, +1.00 MHz and +0.87 MHz for B2, and 0.00 MHz and +0.53 MHz for B3. The experimental and simulated angles, θ and φ, are also very similar. Thus, there appears to be good agreement between the calculated and observed constants, despite the very small values for both A_{iso} and B.

The final defect we consider is I_{CN} for which the EPR constants are listed in the bottom row of Table II, where both the experimental and calculated values of the B tensor are seen to be slightly larger than those of $I_C I_N$. However, unlike the latter defect, there are appreciable differences between the calculated and experimental constants, both in magnitude and sign, where the closest numbers, these for B3, are −0.034 MHz and +0.07 MHz. One common feature is that the predicted value of A_{iso} and that deduced from experiment are both substantially larger than the components of B, which is unique among the four interstitial defects. The difference between the two values for A_{iso}, where the prediction is 75% greater than experiment, together with the lack of agreement for any of the components of B, calls into doubt the attribution of the experimental constants to I_{CN}.

C. IR vibrational analysis

The vibration spectrum of pristine diamond is particularly straight forward since, for reasons of symmetry, there are no IR active modes and just a single Raman peak at 1332 cm^{-1},[46] corresponding to the first-order scattering of triply degenerate TO(X) phonons of t_{2g}. This compares with a value of 1317 cm^{-1} (−1%) derived from the B3LYP functional and modified Pople basis set here adopted. Therefore, all observed IR peaks and Raman peaks, other than that at 1332 cm^{-1}, in the spectra of the three defective systems investigated here, can be assigned unambiguously to the presence of the impurity defects.

Experimental IR and Raman spectra have been collected by several authors cited above.[25–27] However, for the most part, they have been used solely as a tool for determining the purity of samples rather than as an additional tool for the characterization of the defects, which has relied largely on interpretations of the EPR data.

The IR spectra of the three defects considered here are shown in Fig. 5, where the vertical lines indicate the positions of the peaks of the single interstitial defects, namely, I_{CC}, I_{NN}, and I_{CN}, which are included for comparison. The corresponding intensities and isotopic shifts are reported in Table III, while graphical animations of the modes are available at www.crystal.unito.it. Together, they represent key tools for the characterization of the various defect modes.

We start by analyzing the IR spectrum of $I_N I_N$, shown in the bottom panel of Fig. 5. Here, there are three dominant peaks at 1431 cm^{-1}, 1542 cm^{-1}, and 1830 cm^{-1}, with intensities of

132 km/mol, 314 km/mol, and 421 km/mol, respectively. There are also three other peaks in the lower wavenumber region of the spectrum at 341 cm^{-1}, 401 cm^{-1}, and 553 cm^{-1}, with intensities of 68 km/mol, 51 km/mol, and 42 km/mol, respectively. All these peaks are related to the *square planar* part of the defective structure defined by A, B, L, and M, as the graphical animation confirms, while Table III indicates that the isotopic shift resulting from the change of mass from ^{14}N to ^{15}N is as large as 36 cm^{-1} and 19 cm^{-1} for the two highest wavenumber modes. By comparison, it is only 6 cm^{-1} for the mode at 341 cm^{-1} and negligible for the others. We posit that the
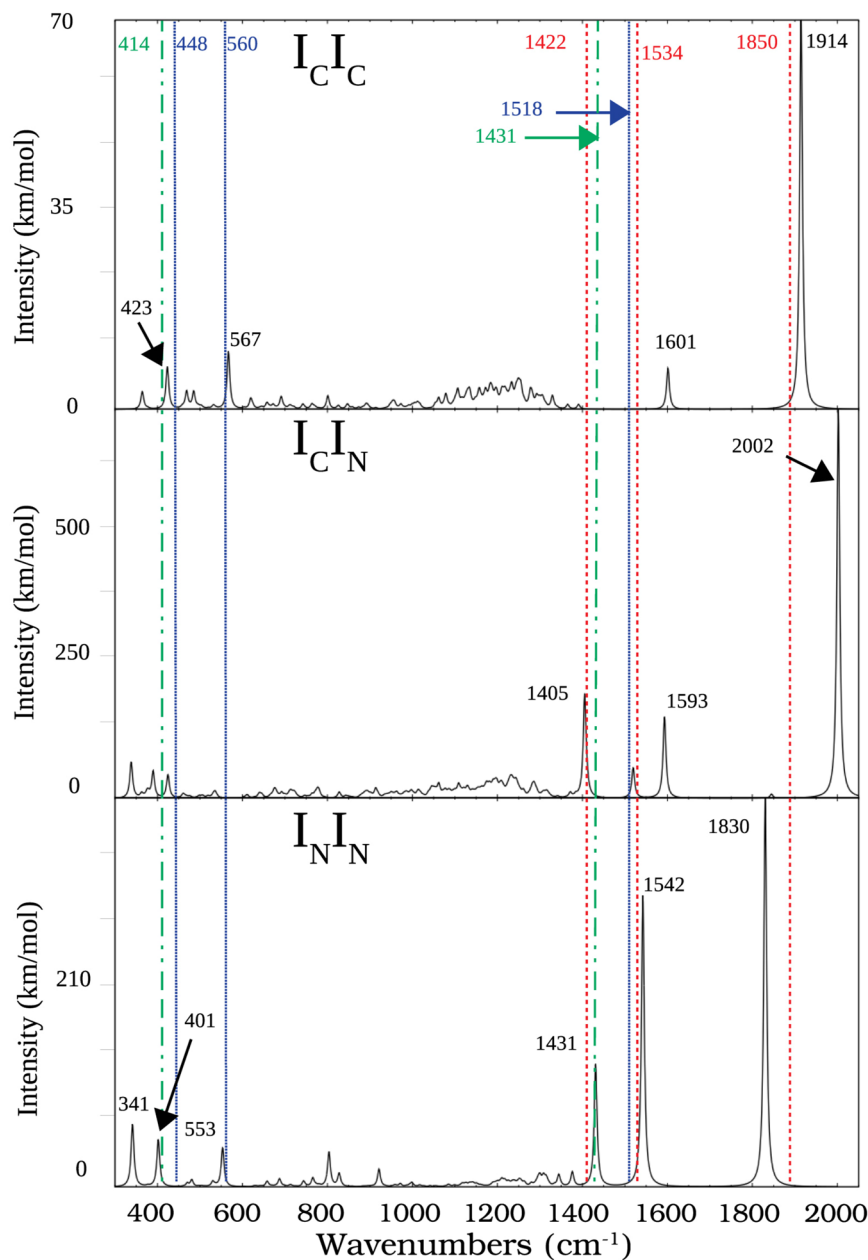

FIG. 5. Simulated IR spectrum of $I_N I_N$ (top), $I_C I_N$ (central), and $I_C I_C$ (bottom) defects. The vertical dashed lines indicate the relevant peaks of I_{CC} (in *blue*), I_{CN} (in *red*), and I_{NN} (in *green*). The intensities of the peaks of both family defects are reported in Table III for better comparison, together with the shifts resulting from the isotopic substitution ^{12}C–^{13}C and ^{14}N–^{15}N.

TABLE III. Wavenumbers (in cm^{-1}) and intensities (in km/mol, in brackets) of the six most intense normal modes of each defect, which are ordered from left to right by decreasing wavenumber. A, B, and L labels of atoms refer to Figs. 1 and 2. For each case, the effect of the isotopic substitution(s) (^{12}C–^{13}C and ^{14}N–^{15}N) is shown. The results are for the a S$_{216}$ supercell.

Defect	Substitution	1	2	3	4	5	6
I$_C$I$_C$	B,L: ^{12}C	1914 (69)	1601 (7)	567 (10)	468 (3)	423 (7)	364 (3)
	B,L: ^{13}C	1870 (66)	1577 (7)	564 (9)	468 (3)	419 (8)	362 (4)
I$_{CC}$	A,B: ^{12}C	1519 (10)	1349 (1)	1338 (3)	1331 (1)	1280 (2)	448 (7)
	A,B: ^{13}C	1490 (9)	1330 (1)	1337 (4)	1331 (1)	1280 (2)	442 (8)
I$_C$I$_N$	B,L: ^{14}N ^{12}C	2002 (751)	1844 (8)	1593 (157)	1405 (198)	425 (45)	390 (51)
	B: ^{15}N	1974 (804)	1841 (436)	1533 (272)	1402 (362)	392 (280)	356 (142)
	L: ^{13}C	1945 (1158)	1854 (115)	1532 (250)	1401 (369)	390 (216)	359 (77)
I$_{CN}$	B,L: ^{14}N ^{12}C	1850 (265)	1534 (86)	1422 (302)	548 (11)	406 (41)	360 (31)
	B: ^{15}N	1823 (254)	1534 (86)	1400 (280)	547 (9)	402 (34)	354 (38)
	L: ^{13}C	1813 (260)	1504 (80)	1422 (302)	547 (11)	406 (41)	359 (30)
I$_N$I$_N$	B,L: ^{14}N	1830 (421)	1542 (314)	1431 (132)	341 (68)	401 (51)	553 (42)
	B,L: ^{15}N	1794 (405)	1523 (250)	1431 (131)	335 (74)	399 (44)	552 (38)
I$_{NN}$	A,B: ^{14}N	1431 (350)	1354 (32)	1346 (23)	550 (29)	414 (102)	364 (44)
	A,B: ^{15}N	1407 (327)	1347 (27)	1346 (27)	549 (24)	409 (89)	360 (58)

high intensity of the defect peaks can be attributed to the large polarity of the bonds involving the N atoms. Now, the I$_N$I$_N$ spectrum can be compared with those of the *simpler* defects, I$_{NN}$ and I$_{CN}$, both of which contain nitrogen. The IR spectrum of I$_{NN}$ is characterized by only two intense peaks (see Table III). The first at 1431 cm^{-1}, with an intensity of 350 km/mol, is exactly the same as that of an I$_N$I$_N$ mode of E symmetry; the second at 414 cm^{-1}, with an intensity of 102 km/mol, is just 13 cm^{-1} above one of the I$_N$I$_N$ peaks, again of E symmetry. In I$_{CN}$, the lower (C$_{2v}$) symmetry activates a CN symmetric stretching mode at 1850 cm^{-1}, with an intensity of 265 km/mol, which is merely 20 cm^{-1} above the highest peak in the I$_N$I$_N$ spectrum. In addition, the E mode of the more symmetric I$_{NN}$ splits into two, giving one at 1534 cm^{-1} (86 km/mol) and one at 1422 cm^{-1} (120 km/mol), which are quite close to the modes at 1542 cm^{-1} and 1431 cm^{-1} of I$_N$I$_N$.

In summary, the three dominant peaks of I$_N$I$_N$ are extremely close to those of I$_{CN}$, with differences 9 cm^{-1}, 8 cm^{-1}, and 20 cm^{-1}, and to two of the modes of I$_{NN}$, with differences 0 cm^{-1} and 13 cm^{-1}.

The symmetric stretch of I$_{CN}$ at 1850 cm^{-1} increases to 2002 cm^{-1} in I$_C$I$_N$, while the intensity increases from 265 km/mol in I$_{CN}$ to 751 km/mol, which is the most intense of all the defects examined here. The two other important peaks are at 1405 cm^{-1} and 1593 cm^{-1}, with intensities of 198 km/mol and 157 km/mol, respectively. The first is 26 cm^{-1} below, and the second is 51 cm^{-1} above the corresponding peak of I$_N$I$_N$. Furthermore, it is of interest to note that the 1405 cm^{-1} peak occurs in a similar region to those of both I$_{NN}$ and I$_{CN}$. A fourth, low intensity absorption is predicted at 1519 cm^{-1}, which is close to those of the two single defects at 1518 cm^{-1} (I$_{CC}$) and 1534 cm^{-1} (I$_{CN}$).

The predicted spectrum of I$_C$I$_C$ is simple, with a single peak of moderate intensity (69 km/mol) at 1914 cm^{-1}, which is intermediate between those of I$_C$I$_N$ at 1830 cm^{-1} and I$_N$I$_N$ at 2002 cm^{-1}. There are also three peaks with much lower intensities. They occur at 1601 cm^{-1} (7 km/mol), which is 8 cm^{-1} above the 1593 cm^{-1} I$_C$I$_N$ peak, at 567 cm^{-1} (I = 10 km/mol, which is close to a similar peak of I$_N$I$_N$), and at 423 cm^{-1} (I = 7 km/mol). The isotopic shift is as large as 44 cm^{-1} for the mode at 1914 cm^{-1} and 24 cm^{-1} for the mode at 1601 cm^{-1} but negligible for the other modes. It is important to note the very different intensity scales in Fig. 5 for the three defects. For interstitial defects with only carbon atom, the polarization of the AB LM bonds is much lower, and the intensities are up to 10 times smaller than for the other defects. The IR spectrum of the third, *single interstitial* defect, I$_{CC}$, is predicted to contain peaks with very low intensities for the reasons discussed above. The peak at 448 cm^{-1} has an intensity of only 14 km/mol and that at 1531 cm^{-1} has an intensity of 20 km/mol so that these peaks are unlikely to be detected in the experimental spectrum with any clarity or precision.

IV. DISCUSSION AND CONCLUSIONS

The principal purpose of this paper is to report, for the first time, all-electron calculations of the Fermi contact term, A_{iso}, and components of the hyperfine coupling tensor, B, of two *single* interstitial defects, I$_{CC}$ and I$_{CN}$, and two *double* interstitial defects, I$_C$I$_N$ and I$_C$I$_C$ (Fig. 1), and to compare these with the reported EPR data.[25–27] Of particular interest are the systems where there are marked disparities between the predicted constants and those derived from the EPR measurements, for which a reasoned

explanation is suggested. Also reported are the IR spectra of the double interstitials, Raman spectra being less useful in view of their very low intensity by comparison with the pristine diamond peak at 1317 cm^{-1}. In addition and for the purpose of exact comparison, the EPR constants of the *single* I_{CN} and I_{CC} interstitial defects (Fig. 2), whose electronic structures and IR spectra have been reported previously,[1,30] have also been included in this study.

As a preliminary comment, we note that IR spectra are able to provide, at least, in principle, information on *all* six defects, whereas EPR can only be used to study open shell systems so that both I_{NN} and $I_N I_N$ are excluded. However, a useful way to by-pass this limitation is to generate the corresponding charged defects, whose ground states might turn out to be open shell, as is the case with VN_2^- and N_2^+ (see Refs. 32 and 33).

We start with $I_C I_C$, for which, as Table II indicates, there is excellent agreement with experiment for the three distinct sets of constants that are obtained from the EPR data, namely, the Fermi contact term, the eigenvalues of the hyperfine coupling tensor B, and the angles, θ and φ, which define the orientation of the principal axes of B with respect to the crystallographic axes. This close agreement between the calculated and observed values of *six* EPR constants attests to the efficacy of the computational methods used in this study. However, perhaps of greater significance in the context of this study is that it leaves no ambiguity in attributing the reported measured constants to the predicted lattice and electronic structures we have assigned to $I_C I_C$. This verification is particularly useful, for the IR spectrum is characterized by peaks of very low intensity since the dipole moments generated by the defect are extremely small. Thus, in spectra of systems containing other defects such as N, which is nearly always present, the $I_C I_C$ peaks would be swamped and certainly not sufficiently visible for identification purposes.

As shown in Table II, the experimental EPR data reported in Ref. 25, purportedly for the single interstitial defect, I_{CC}, are very close to that for $I_C I_C$, but only in part. For while there is very good agreement with our predicted values of the hyperfine coupling tensor, B, for the two interstitial defects, with an average deviation across the three components of 2%, the values of the Fermi contact term, A_{iso}, are quite different, with an observed value of 44 MHz compared with a prediction of 25.4 MHz. Since the double interstitial is the more stable of the two defects, it is entirely possible that samples of I_{CC} might be contaminated by low concentrations of $I_C I_C$ so that the EPR spectrum attributed to I_{CC} by Hunt[25] is, in fact, that of $I_C I_C$. Our calculations would certainly support this possibility, which new EPR experiments might help to clarify. In the absence of such data, the IR spectra might be useful here, for the I_{CC} 1518 cm^{-1} peak, though weak (10 km/mol), is separated by 83 cm^{-1} from that at 1601 cm^{-1} in the $I_C I_C$ spectrum, which is also weaker.

We note that the IR spectrum is of little value here for the confirming the presence of I_{CC} since all the predicted defect peaks have even lower intensities, 10 km/mol or less, than those for $I_C I_C$, the least intense of which is calculated to be 69 km/mol. Turning now to the N-containing interstitials, as shown in Fig. 2 (b), the distance between the N atom (B) and the C atom with the unpaired spin (L) in $I_C I_N$ is appreciably larger than the normal lattice spacing, leading to a weak spin–spin interaction with the ^{15}N nucleus. This is reflected in the very small values of both the measured and calculated

values of A_{iso} and B, as indicated in Table II, where the *differences* between these for the components of B are comparable to those for $I_C I_C$ and I_{CC}. Unlike the pure carbon interstitials, no such ambiguity can arise in the case of $I_C I_N$ as to the attribution of the EPR constants, since I_{NN} is spin inactive. In view of this, any uncertainty in identifying the experimental EPR spectrum with the microscopic structure that we indicate as $I_C I_N$ is much less certain. It might also be worth noting that in the absence of isotope enrichment, the natural abundance of ^{13}C is ~30 times that of ^{15}N. What might clarify this issue is the IR spectrum, for, as Fig. 5 indicates, the $I_C I_N$ spectrum contains an intense (751 km/mol) peak at 2002 cm^{-1}, which is separated by 90 cm^{-1} from all the other interstitial peaks. To date, there are no reports of the experimental spectrum.

In the case of I_{CN}, we find very substantial differences between the predicted values of A_{iso} and B and those reported by Felton *et al.* from their EPR data, with errors of 55% for A_{iso} and over 200% for the B_1 and B_2 components of B. In view of the good accord for other systems and the reliability of our computational procedures, more generally, we suggest that the experimental results might not relate to the I_{CN} structure we have derived in this study. Here again, the IR spectrum is of potential value in characterizing this defect, for the predicted intense (265 km/mol) peak at 1850 cm^{-1} is sufficiently separated from that of $I_N I_N$ at 1830 cm^{-1} (421 km/mol) and well separated from those of the other defects. The final two interstitials we have examined are I_{NN} and $I_N I_N$, which have closed shell ground states, and are, consequently, EPR inactive. The only recourse to the hyperfine coupling constants, therefore, would be via their charged states, which, to date, appear not to have been examined. However, there are major differences in the predicted IR spectra of the two interstitials, which might be exploited. The predicted $I_N I_N$ spectrum contains two intense peaks, one at 1830 cm^{-1} (I = 421 km/mol) and the other at 1541 (I = 314 km/mol), whereas the spectrum of I_{NN} exhibits a single strong peak at 1431 cm^{-1} (I = 350 km/mol). Since the latter is roughly 20 times the intensity of the peak in the $I_N I_N$ spectrum with exactly the same frequency, there would seem to be little by way of confusion. I_{CN} has a peak at 1422 cm^{-1}, but these can be distinguished using ^{15}N isotopic shifts. Again, to date, there appears to be no experimental IR data for these defects or for I_{CN}.

In summary, this study has shown that spectroscopies such as IR and EPR, while extremely informative for some defect systems, when used singly, can be restricted in the information they are able to provide for others. On the other hand, the combination of IR, EPR, and simulations, based on high-level quantum mechanical calculations, can provide a comprehensive, unified, and consistent description of the microscopic structural, dynamic, and electronic properties of a much wider range of materials.

The specific conclusions of this study are as follows:

- $I_C I_C$ can be uniquely identified by its observed EPR constants.
- The close similarity of the reported experimental values of the anisotropic term, **B**, of I_{CC} and $I_C I_C$, in conjunction with the calculations reported here, raises questions as to the correct attribution of the EPR data for I_{CC}.
- The very low values of the experimental and predicted EPR constants of $I_C I_N$, which result from weak spin–spin interactions, for structural reasons, suggest that these alone do not

provide strong evidence for the identity of this defect and that the experimental IR spectrum would make an important contribution to this.

- The experimental EPR constants of I_{CN} might not relate to the lattice and electronic structures we have calculated for this defect, but the reliable IR data might clarify this issue.
- In the absence of charged species of I_{NN} and $I_N I_N$, from which EPR constants might be obtained, the differences in their predicted IR spectra suggest that the experimental spectra could provide a useful and accurate means of identification.

ACKNOWLEDGMENTS

DATA AVAILABILITY

The data that support the findings of this study are available within the article.

REFERENCES

[1] S. Salustro, F. Pascale, W. C. Mackrodt, C. Ravoux, A. Erba, and R. Dovesi, Phys. Chem. Chem. Phys. **20**, 16615 (2018).

[2] J. P. Bade, S. R. Sahaida, B. R. Stoner, J. A. Von Windheim, J. T. Glass, K. Miyata, K. Nishimura, and K. Kobashi, Diamond Relat. Mater. **2**, 816 (1993).

[3] P. Bergonzo, D. Tromson, and C. Mer, J. Synchrotron Radiat. **13**, 151 (2006).

[4] G. Aiello, T. Scherer, K. Avramidis, N. Casal, T. Franke, M. Gagliardi, G. Gantenbein, M. Henderson, J. Jelonnek, A. Meier et al., Fusion Sci. Technol. **75**, 719 (2019).

[5] S. J. Breuer and P. R. Briddon, Phys. Rev. B **51**, 6984 (1995).

[6] F. Gentile, S. Salustro, G. Di Palma, M. Causá, P. D'arco, and R. Dovesi, Theor. Chem. Acc. **137**, 154 (2018).

[7] A. Mainwood, Diamond Relat. Mater. **8**, 1560 (1999).

[8] J. P. Goss, B. J. Coomer, R. Jones, C. J. Fall, P. R. Briddon, and S. Öberg, Phys. Rev. B **67**, 165208 (2003).

[9] S. Salustro, F. Colasuonno, A. M. Ferrari, M. D'Amore, W. C. Mackrodt, and R. Dovesi, Carbon **146**, 709 (2019).

[10] D. J. Twitchen, D. C. Hunt, M. E. Newton, J. M. Baker, T. R. Anthony, and W. F. Banholzer, Phys. B: Condens. Matter **273-274**, 628 (1999).

[11] H. Amekura and N. Kishimoto, J. Appl. Phys. **104**, 063509 (2008).

[12] D. N. Jamieson, S. Prawer, K. W. Nugent, and S. P. Dooley, Phys. Rev. B **106**, 641 (1995).

[13] A. Gali, Phys. Rev. B **79**, 235210 (2009).

[14] T. Schröder, M. E. Trusheim, M. Walsh, L. Li, J. Zheng, M. Schukraft, A. Sipahigil, R. E. Evans, D. D. Sukachev, C. T. Nguyen et al., Nat. Commun. **8**, 15376 (2017).

[15] A. Mainwood, J. Phys. C: Solid State Phys. **11**, 2703 (1978).

[16] U. Gerstmann, M. Amkreutz, and H. Overhof, Phys. Rev. B **60**, R8446 (1999).

[17] J. A. van Wyk, O. D. Tucker, M. E. Newton, J. M. Baker, G. S. Woods, and P. Spear, Phys. Rev. B **52**, 12657 (1995).

[18] A. Zelferino, S. Salustro, J. Baima, V. Lacivita, R. Orlando, and R. Dovesi, Theor. Chem. Acc. **135**, 74 (2016).

[19] J. P. Goss, B. J. Coomer, R. Jones, T. D. Shaw, P. R. Briddon, M. Rayson, and S. Öberg, Phys. Rev. B **63**, 195208 (2001).

[20] G. Davies, H. Smith, and H. Kanda, Phys. Rev. B **62**, 1528 (2000).

[21] J. P. Goss, R. Jones, T. D. Shaw, M. J. Rayson, and P. R. Briddon, Phys. Status Solidi A **186**, 215 (2001).

[22] M. E. Newton, B. A. Campbell, D. J. Twitchen, J. M. Baker, and T. R. Anthony, Diamond Relat. Mater. **11**, 618 (2002).

[23] S. Salustro, Y. Nöel, C. M. Zicovich-Wilson, P. Olivero, and R. Dovesi, J. Chem. Phys. **145**, 184701 (2016).

[24] O. D. Tucker, M. E. Newton, and J. M. Baker, Phys. Rev. B **50**, 15586 (1994).

[25] D. Hunt, D. Twitchen, M. Newton, J. Baker, J. Kirui, J. van Wyk, T. Anthony, and W. Banholzer, Phys. Rev. B **62**, 6587 (2000).

[26] D. J. Twitchen, M. E. Newton, J. M. Baker, O. D. Tucker, T. R. Anthony, and W. F. Banholzer, Phys. Rev. B **54**, 6988 (1996).

[27] S. Felton, B. L. Cann, A. M. Edmonds, S. Liggins, R. J. Cruddace, M. E. Newton, D. Fisher, and J. M. Baker, J. Phys.: Condens. Matter **21**, 364212 (2009).

[28] R. Dovesi, A. Erba, R. Orlando, C. M. Zicovich-Wilson, B. Civalleri, L. Maschio, M. Rérat, S. Casassa, J. Baima, S. Salustro et al., Wires **8**, e1360 (2018).

[29] R. Dovesi, V. R. Saunders, C. Roetti, R. Orlando, C. M. Zicovich-Wilson, F. Pascale, B. Civalleri, K. Doll, N. M. Harrison, I. J. Bush et al., CRYSTAL 2017 User's Manual (University of Torino, Torino, 2017).

[30] S. Salustro, A. Erba, C. M. Zicovich-Wilson, Y. Nöel, L. Maschio, and R. Dovesi, Phys. Chem. Chem. Phys. **18**, 21288 (2016).

[31] A. M. Ferrari, S. Salustro, F. S. Gentile, W. C. Mackrodt, and R. Dovesi, Carbon **134**, 354 (2018).

[32] G. Di Palma, B. Kirtman, F. S. Gentile, A. Platonenko, A. M. Ferrari, and R. Dovesi, Carbon **159**, 443 (2020).

[33] G. Di Palma, F. S. Gentile, V. Lacivita, W. Mackrodt, R. Dovesi et al., J. Mater. Chem. C **8**, 5239 (2020).

[34] A. D. Becke, J. Chem. Phys. **98**, 5648 (1993).

[35] C. Lee, W. Yang, and R. G. Parr, Phys. Rev. B **37**, 785 (1988).

[36] J. S. Binkley, J. A. Pople, and W. J. Hehre, J. Am. Chem. Soc. **102**, 939 (1980).

[37] H. Kjær and S. S. P. Sauer, J. Chem. Theory Comput. **7**, 4070 (2011).

[38] A. D. Becke, J. Chem. Phys. **88**, 2547 (1988).

[39] H. J. Monkhorst and J. D. Pack, Phys. Rev. B **13**, 5188 (1976).

[40] F. Pascale, C. M. Zicovich-Wilson, F. López Gejo, B. Civalleri, R. Orlando, and R. Dovesi, J. Comput. Chem. **25**, 888 (2004).

[41] S. Dall'Olio, R. Dovesi, and R. Resta, Phys. Rev. B **56**, 10105 (1997).

[42] R. D. King-Smith and D. Vanderbilt, Phys. Rev. B **49**, 5828 (1994).

[43] H. E. Smith, G. Davies, M. E. Newton, and H. Kanda, Phys. Rev. B **69**, 045203 (2004).

[44] M. Cardona and M. L. W. Thewalt, Rev. Mod. Phys. **77**, 1173 (2005).

[45] D. C. Hunt, D. J. Twitchen, M. E. Newton, J. M. Baker, T. R. Anthony, W. F. Banholzer, and S. S. Vagarali, Phys. Rev. B **61**, 3863 (2000).

[46] S. Prawer and R. J. Nemanich, Philos. Trans. R. Soc., A **362**, 2537 (2004).